

The Role of Asparagine as a Gatekeeper Residue in the Selective Binding of Rare Earth Elements by Lanthanide-Binding Peptides

Surabh S. KT,^[a] Baofu Qiao,^{*[b]} Jason G. Marmorstein,^[c] Yiming Wang,^[d, e] Denize C. Favaro,^[f] Kathleen J. Stebe,^[d] E. James Petersson,^[c] Ravi Radhakrishnan,^[d, e] Cesar de la Fuente-Nunez,^[d, e, g] Raymond S. Tu,^[a] Charles Maldarelli,^[a] Monica Olvera de la Cruz,^{*[h]} and Robert J. Messinger^{*[a]}

Lanthanide-binding tag (LBT) peptides selectively complex lanthanide cations (Ln^{3+}) in their binding pockets and are promising for lanthanide separation. However, designing LBTs that selectively target specific Ln^{3+} cations remains a challenge due to limited molecular-level understanding and control of interactions within the lanthanide-binding pocket. In this study, we reveal that the N5 asparagine residue acts as a gatekeeper in the binding pocket, resulting in a 100-fold selectivity for smaller Lu^{3+} over larger La^{3+} cations. Nuclear magnetic resonance spectroscopy and molecular dynamics simulations show that the N5 residue weakly binds to the larger La^{3+} cation, permitting H_2O molecules inside the pocket. For the smaller Lu^{3+} cations, the

N5 residue forms an inter-arm hydrogen bond with the E14 glutamic acid residue, locking the Lu^{3+} cation in the pocket and preventing H_2O infiltration. Mutating the N5 asparagine to a D5 aspartic acid prevents such a hydrogen bond, eliminating the gatekeeping mechanism and precipitously reducing selectivity. The resulting binding affinity to Ln^{3+} cations is non-monotonic but generally increases with cation size. These results suggest a molecular design paradigm: the reduced affinity for larger lanthanides is due to open pocket conformations, while the selectivity of smaller Ln^{3+} cations over larger ones is due to the gatekeeping hydrogen bond.

1. Introduction

Rare earth elements (REEs), encompassing scandium, yttrium, and the 15 lanthanides from lanthanum (La) to lutetium (Lu), are crucial elements owing to their unique magnetic, luminescent, and catalytic properties.^[1–4] They play an integral role in diverse technological applications, ranging from smartphones, optical displays, catalysts to various alloys.^[5,6] Furthermore, they

are indispensable for clean energy technologies (wind turbines, batteries, lighting systems, etc.) and are recognized as commodities with substantial future demand.^[7–9] However, the separation of individual REEs from feedstocks poses a significant challenge due to inherent similarities in physicochemical properties. These elements predominantly exhibit a +3 oxidation state, rendering charge-based separations ineffective. Additionally, the minimal decrease in cation radius of 0.19 Å across the

[a] S. S. KT, Prof. R. S. Tu, Prof. C. Maldarelli, Prof. R. J. Messinger
Department of Chemical Engineering, The City College of New York, CUNY,
160 Convent Ave, New York, NY 10031, USA
E-mail: rmessinger@ccny.cuny.edu

[b] Prof. B. Qiao
Department of Natural Sciences, Baruch College, City University of New York,
55 Lexington Ave, New York, NY 10010, USA
E-mail: baofu.qiao@baruch.cuny.edu

[c] J. G. Marmorstein, Prof. E. J. Petersson
Department of Chemistry, University of Pennsylvania, 231 S 34th St,
Philadelphia, PA 19104, USA

[d] Dr. Y. Wang, Prof. K. J. Stebe, Prof. R. Radhakrishnan, Prof. C. de la Fuente-Nunez
Department of Chemical and Biomolecular Engineering, University of
Pennsylvania, 311A, 220 S 33rd St Towne Building, Philadelphia, PA 19104, USA

[e] Dr. Y. Wang, Prof. R. Radhakrishnan, Prof. C. de la Fuente-Nunez
Department of Bioengineering, University of Pennsylvania, 240 Skirkanich
Hall, 210 S 33rd St, Philadelphia, PA 19104, USA


[f] Dr. D. C. Favaro
Structural Biology Initiative, CUNY Advanced Science Research Center, 85 St
Nicholas Terrace, New York, NY 10031, USA

[g] Prof. C. de la Fuente-Nunez
Departments of Microbiology and Psychiatry, Robert Wood Johnson
Pavilion, University of Pennsylvania, Philadelphia, PA 19104, USA

[h] Prof. M. Olvera de la Cruz
Department of Material Science and Engineering, Northwestern University,
Room 2036, Cook Hall, 2220 Campus Drive, Evanston, IL 60208, USA
E-mail: m-olvera@northwestern.edu

Surabh S. KT and Baofu Qiao contributed equally to this work.

 Supporting information for this article is available on the WWW under
<https://doi.org/10.1002/chem.202501318>

 © 2025 The Author(s). Chemistry – A European Journal published by
Wiley-VCH GmbH. This is an open access article under the terms of the
Creative Commons Attribution-NonCommercial-NoDerivs License, which
permits use and distribution in any medium, provided the original work is
properly cited, the use is non-commercial and no modifications or
adaptations are made.

lanthanide series from La to Lu is difficult to exploit.^[10] Conventional REE separation methods, such as solvent extraction, are characterized by extensive energy consumption, large volumes of extractants, the necessity of multiple stages for complete purification, and potential environmental issues due to reliance on organophosphates.^[11,12] Addressing these concerns is a significant focus of current research efforts, driving the advancement of sustainable REE separation chemistries.

Biomolecular approaches utilizing Ln^{3+} -binding proteins or peptides are appealing for REE recovery owing to their high affinity, selectivity, an all-aqueous separation platform, and minimal energy requirements.^[13,14] This has spurred research to exploit such proteins in separation schemes. For instance, enhanced REE adsorption was observed by genetically displaying EF-hand binding motifs in intact proteins on cell surfaces^[15–19] or in the extracellular matrices^[20] of bacteria. The recent discovery of the Ln^{3+} -binding protein Lanmodulin (LanM) in methylotrophic bacteria with its picomolar affinity for Ln^{3+} introduces another compelling option for REE separation.^[21,22] Prior studies have exploited LanM immobilized on magnetic nanoparticles,^[23] displayed on fungal/bacterial cell surfaces,^[24,25] and incorporated into elastin-like polypeptides^[26] to effectively concentrate REEs from other competing metals present in feedstocks. In addition, LanM tethered on agarose beads has demonstrated selective separation of the commercially important Nd^{3+} - Dy^{3+} pair.^[27,28] More recent efforts have focused on peptides that incorporate the EF-hand binding motifs in separation schemes. These studies are motivated in part by atom economy, a significant advance if the smaller peptides can recapitulate or even enhance the selectivity of the EF-hand structures in intact proteins. For example, peptides derived from the EF-hand loops of LanM have been immobilized on gold nanoparticles and utilized to bind and separate REEs,^[29,30] albeit the isolation of the Ln^{3+} -binding loop sequence is associated with a significant decrease in dissociation constants (K_d) from picomolar to micromolar regime.^[31] Lanthanide-binding tags (LBTs) are peptides engineered from EF-hand motifs of calcium metalloproteins like Calmodulin and Troponin C; these peptides have shown nanomolar affinity for Ln^{3+} cations (Scheme 1A).^[32] While LBTs were initially developed as bioprobes, harnessing the luminescent and paramagnetic properties of Ln^{3+} cations,^[33–37] they have recently been repurposed for the capture and separation of REEs. Ortuno Macias et al.^[38] focused on these peptides and demonstrated that LBTs can be rationally mutated to enhance surface activity, exhibiting a twofold selectivity to Tb^{3+} over La^{3+} cations at the air–water interface.

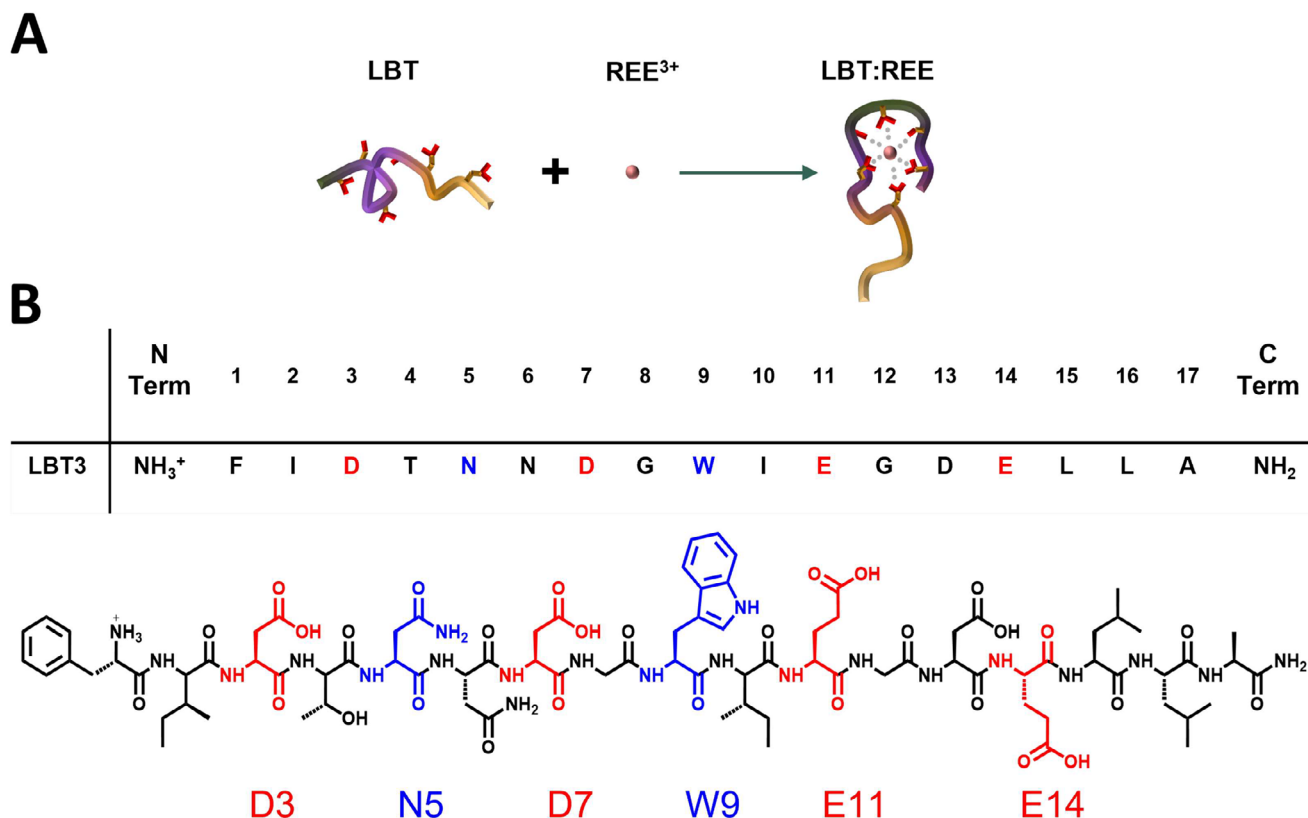
As biomolecular motifs continue to advance in REE selective separation technologies, there is a growing need to gain molecular-level insights into their ability to distinguish among the REEs. Very few studies have explored the structure–selectivity relationship to enable the complex separation of Ln^{3+} across the lanthanide series. Nitz et al.^[39] had presented the X-ray crystal structure of an LBT- Tb^{3+} complex, revealing the ligating amino acid residues and that water was excluded in the Tb^{3+} coordination environment. Interestingly, Hatanaka et al.^[40] demonstrated that water infiltration into the binding pocket of the LBT3 peptide occurs for lighter (larger) lanthanides

(e.g., La^{3+}), reducing affinity. Hence, it is critical to characterize and understand the molecular-level structures, interactions, and dynamics within the binding loops of Ln^{3+} -binding peptides to design peptide sequences to control selectively for a preferred Ln^{3+} cation. In this study, building upon previous work of Hatanaka et al.,^[40] we elucidate how binding selectivity is determined by Ln^{3+} cation size through a previously unidentified hydrogen bonding interaction between residues, which acts as a “gatekeeping” mechanism. Specifically, using the LBT3 peptide (sequence: NH_3^+ -FIDTNDGWIEGDELLA- NH_2 , Scheme 1B), we investigated the structures, interactions, and dynamics of the binding loop upon complexation with larger La^{3+} and smaller Lu^{3+} cations at a molecular level. By coupling advanced NMR and molecular dynamics (MD) methods, we demonstrate that LBT3: Ln^{3+} complexes adopt multiple binding conformations. Notably, the N5 asparagine residue, which is a weaker binding residue, undergoes partial or complete dissociation depending on the Ln^{3+} cation size. For larger La^{3+} cations, the N5 residue only weakly binds to the cation, enabling an H_2O molecule to infiltrate the binding pocket and leading to lower LBT3- La^{3+} binding affinity. For smaller Lu^{3+} cations, the N5 residue dissociates with the cation but instead hydrogen bonds to the E14 glutamic residue in the pocket, locking the Lu^{3+} cation in the pocket, preventing H_2O infiltration, and increasing LBT3- Lu^{3+} binding affinity. These changes in binding, in combination with H_2O exclusion, lead to a 100-fold higher selectivity for Lu^{3+} over La^{3+} , as evidenced by the measured thermodynamic dissociation constants K_d . Hence, the N5 asparagine residue acts as a “gatekeeper” residue. Furthermore, mutation of the N5 asparagine to a D5 aspartic acid residue is shown to significantly reduce Ln^{3+} selectivity, despite preserving high binding affinity, underscoring the critical role of the asparagine within the binding pocket in size-based Ln^{3+} cation recognition. Overall, our findings shed light on the interplay between peptide conformational dynamics and lanthanide ion coordination, providing valuable insights for the design of more efficient and selective LBT-based systems for REE separations.

2. Results and Discussion

2.1. Cation-Dependent Chemical Exchange Rates in LBT3- Ln^{3+} Complexes

^1H NMR titration measurements were conducted to experimentally assess LBT3's affinity for trivalent rare earth cations and its capability to distinguish between them despite their subtle size differences. Varying concentrations of La^{3+} and Lu^{3+} were systematically introduced into a 100 μM LBT3 solution to probe the conformational changes associated with complexation at different LBT3: Ln^{3+} molar ratios. La^{3+} and Lu^{3+} were chosen not only for the different sizes but also due to their diamagnetic nature. Other lanthanide cations are paramagnetic, which leads to extensive line broadening and loss of signal intensity due to paramagnetic relaxation enhancement effects. The ^1H NMR titration spectra revealed marked differences in dynamics between the LBT3- La^{3+} and LBT3- Lu^{3+} complexes. The introduction of La^{3+}



Scheme 1. (A) Schematic representation of an LBT peptide binding to a rare earth cation. (B) Sequence and chemical structure of LBT3 peptide used in this study. The highlighted amino acids represent the ligating residues.

to 100 μM LBT3 (Figure 1A) resulted in a pronounced broadening of the peptide ^1H signals within the amide region for $\text{La}^{3+}:\text{LBT3}$ ratios below 1. For $\text{La}^{3+}:\text{LBT3}$ molar ratio ≥ 1 , distinct ^1H signals corresponding to the complexed state emerged. Notably, at a $\text{La}^{3+}:\text{LBT3}$ molar ratio of 2:1, the ^1H signals corresponding to the complexed state are resolved completely.

Conversely, upon titrating Lu^{3+} cations into 100 μM LBT3 (Figure 1B), new ^1H signals for the $\text{LBT3}:\text{Lu}^{3+}$ complex were resolved even at the lowest concentrations tested. As the Lu^{3+} concentration increased, the intensity of the ^1H signals associated with the $\text{LBT3}:\text{Lu}^{3+}$ complex increased with a concurrent reduction in the ^1H signal intensities due to unbound LBT3. This trend reflected a clear shift towards the complexed state as the concentration of Lu^{3+} increases. As the $\text{Lu}^{3+}:\text{LBT3}$ ratio reached 2:1, all ^1H signals corresponding to the unbound LBT3 vanished, affirming the complete transition to the bound state.

The broadening observed in the LBT3 amide ^1H signals upon titration with La^{3+} cations suggests an intermediate chemical exchange regime between the bound and unbound states. This phenomenon occurs when the proton's chemical exchange rates between the two signals, such as those associated with the bound and unbound states, are comparable to the differences in their NMR frequencies. With an excess of La^{3+} , complete complexation occurs, yielding sharper ^1H amide signals. In contrast, upon the addition of Lu^{3+} cations, the co-existing ^1H signals associated with bound and unbound states observed at $\text{Lu}^{3+}:\text{LBT3}$ ratios < 1 signify a slow chemical exchange regime. This regime indicates slower dissociation kinetics where the time

scale of exchange between the bound and unbound states is much slower than the differences in their NMR frequencies. These findings are consistent with the results of Hatanaka et al.,^[40] suggesting that the $\text{LBT3}:\text{Lu}^{3+}$ complex is more tightly bound compared to the $\text{LBT3}:\text{La}^{3+}$ complex. As shown below, Lu^{3+} displays a greater LBT3 binding affinity than La^{3+} , consistent with these observations.

2.2. 3D Molecular Structure of $\text{LBT3}:\text{La}^{3+}$ Complex by NMR

The distinct difference in binding affinity between La^{3+} and Lu^{3+} with LBT3 was also reflected in specific 3D structural features of the binding loop obtained from multidimensional solution-state NMR measurements. To establish spatial constraints, ^1H distance restraints were derived from the 2D $^1\text{H}-^1\text{H}$ NOESY spectra at 25 $^\circ\text{C}$ using the CYANA calibration. The ^1H , ^{13}C , and ^{15}N chemical shift values were obtained from $^1\text{H}-^{13}\text{C}$ HSQC (Figure S1), $^1\text{H}-^{15}\text{N}$ HSQC (Figure S2), $^1\text{H}-^1\text{H}$ TOCSY (Figure S3), and $^1\text{H}-^1\text{H}$ NOESY (Figure S4). The top 20 structures from CYANA were refined by simulated annealing for 100 ns under restraints. This extended duration, compared to the shorter time of 20 ps used by Hatanaka et al.,^[40] allowed us to explore energetically similar populations more thoroughly. Following refinement, the top 20 structures (Figure 2) exhibited populations with diverse coordination environments. Across these structures, the total coordination number (CN) of La^{3+} consistently remained at 10. The most predominant conformation (Figure 2A) demonstrated

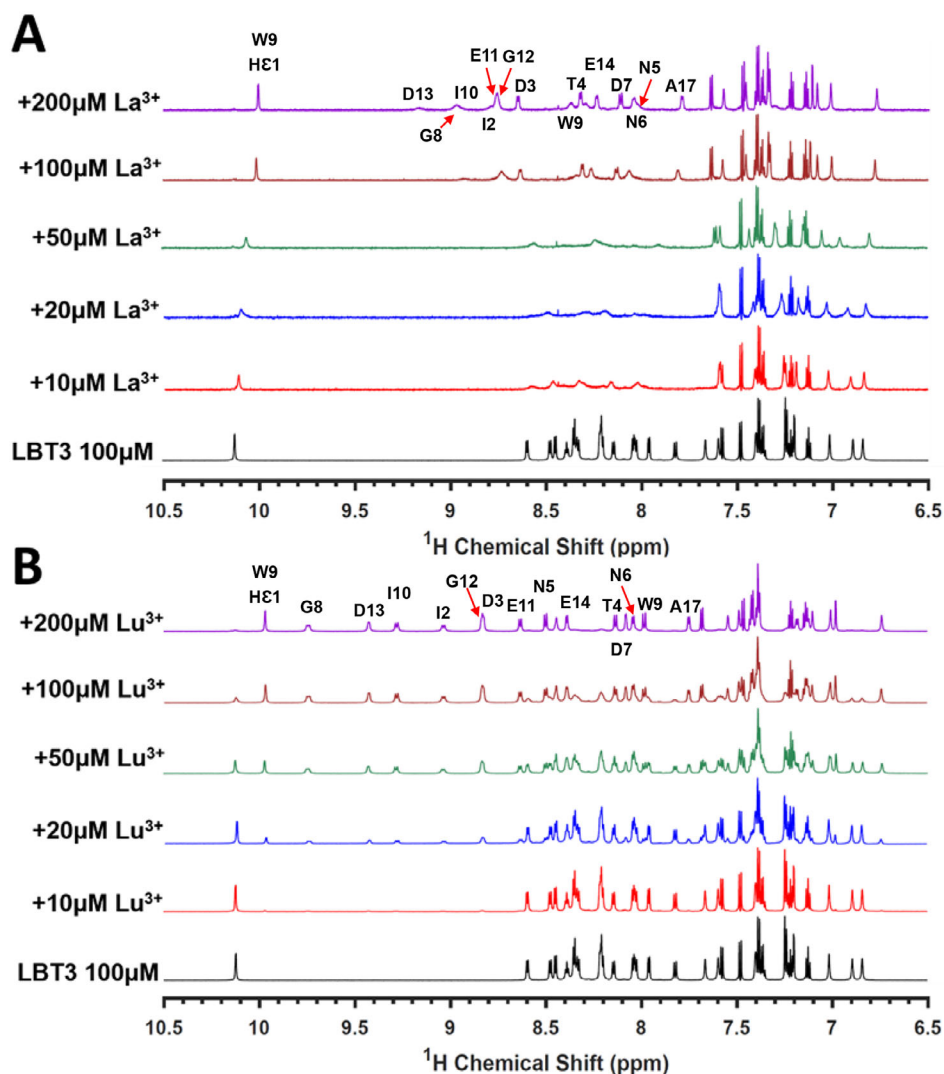


Figure 1. Differential Ln^{3+} binding affinities of the LBT3 peptide observed through solution-state ^1H single-pulse NMR measurements. Quantitative ^1H single-pulse NMR spectra (amide region) acquired at 25 $^{\circ}\text{C}$ with varying concentrations of (A) La^{3+} and (B) Lu^{3+} cations titrated into 100 μM LBT3 in 50 mM MES- d_{13} buffer ($\text{H}_2\text{O}:\text{D}_2\text{O}$ volume ratio of 90:10).

a bidentate ligation of D3, D7, E11, and E14 residues, whereas N5 and W9 exhibited monodentate ligation. Intriguingly, a notable subset of structures revealed a distinct scenario where the N5 residue appeared dissociated (Figure 2B). In these instances, a water molecule, instead of the N5 residue, was engaging in direct coordination with the La^{3+} cation.

Furthermore, conformations with more than one H_2O molecule in the binding loop were also observed (Figure 2C). Within these structures, the N5 and W9 residues were completely dissociated, and the D7 transitioned from a bidentate to monodentate ligation. These conformations observed for the LBT3- La^{3+} complex stem from the dissociation of residues like N5 and W9, which form weaker coordination with the La^{3+} cation compared to the robust electrostatic interactions observed with the other residues (D3, D7, E11, and E14). In contrast, the unbound LBT3 exhibited a random coil structure (Figure 2D). Overall, the varied coordination environments observed highlight the structural diversity of the LBT3- La^{3+} complex. These results furthermore suggest that the binding affinity

of Ln^{3+} to LBT3 hinges on the extent of residue dissociation and concurrent water infiltration into the LBT binding pocket, reflecting the interplay between residue binding strengths and the accommodating pocket size relative to the cation.

2.3. LBT3- Ln^{3+} Complexes: N5 Dissociation and Water Infiltration

To explore how cation selectivity relates to the peptide's structural dynamics, particularly regarding residue dissociation and water infiltration, we conducted unbiased all-atom MD (AA-MD) simulations on the LBT3- La^{3+} and LBT3- Lu^{3+} complexes. Three parallel runs were conducted for each complex. They converged after a simulation time of 2.5 μs for La^{3+} and 3 μs for Lu^{3+} (Figure S5), necessitating the long simulation duration of 6 μs for each run. The initial conformation utilized in these simulations reflected the predominant NMR conformation, featuring D3, N5, D7, W9, E11, and E14 as binding residues. Throughout

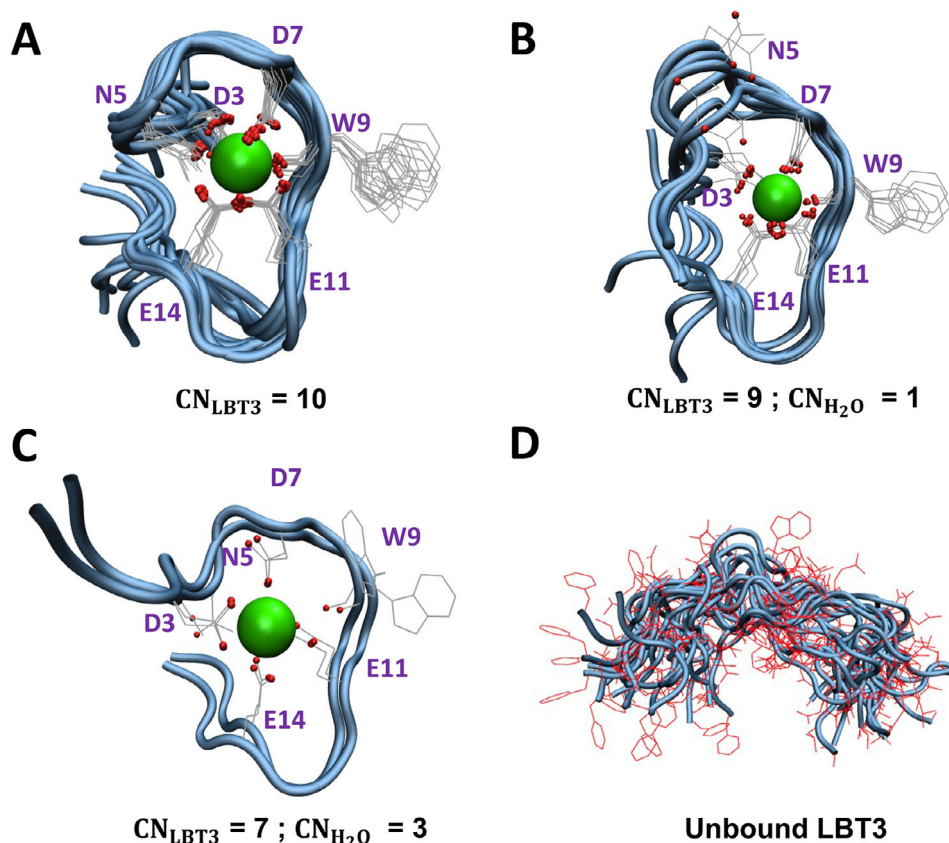


Figure 2. Top 20 refined NMR structures of the LBT3- La^{3+} complex exhibiting different populations with varying coordination environments of La^{3+} cation (A) $CN_{LBT3} = 10$ (B) $CN_{LBT3} = 9$, $CN_{H_2O} = 1$ and (C) $CN_{LBT3} = 7$, $CN_{H_2O} = 3$. Here CN_x represents the contribution of x ligand toward the total coordination number (CN) of La^{3+} ; water molecules are not depicted for visualization. The top 20 NMR structures of unbound LBT3 are shown in (D).

these long-time-scale simulations, we observed the dissociation of the N5 residue in both the LBT3- La^{3+} and LBT3- Lu^{3+} complexes. Specifically, throughout the simulation, we observed a progressive increase in distance between the La^{3+} cation and the oxygen atom on the carbonyl group of the N5 residue OD1(N5), where “D” indicates that the oxygen atom is the delta position (Figure 3A). This distance expanded from 2.6 Å, representative of the bound state, to an intermediate distance of 5 Å corresponding to partial dissociation. On closer examination, the partial dissociation facilitated the infiltration of a water molecule into the binding pocket. While coordinated with the La^{3+} ion, this infiltrated water molecule engaged in hydrogen bonding with the N5 residue via the sidechain OD1 atom, resulting in this intermediate state. As the simulations progressed beyond 2.5 μ s, all three runs consistently demonstrated complete dissociation of the N5 residue, as evidenced by the La^{3+} -OD1(N5) distance extending to 11.2 Å. The final simulation structure is represented in Figure S6. Additionally, using the last 2 μ s of the simulation trajectories, we analyzed the La^{3+} coordination environment. The tabulated values in Table S1 revealed that across all three runs, D3, D7, E11, and E14 displayed bidentate ligation, while W9 exhibited monodentate ligation. Notably, the infiltrated water also contributed to the total coordination number of La^{3+} by 1, resulting in a total of 10, consistent with the NMR structures.

In contrast, the Lu^{3+} -N5 coordination displayed a binary mode for the smaller Lu^{3+} ion such that the average Lu^{3+} -

OD1(N5) distance jumped from 2.3 Å in the initial conformation to an average distance of 6.5 Å (Figure 3B). This converged state resembled the intermediate state observed for the LBT3- La^{3+} complex where the N5 residue remained directed inside the pocket. But for Lu^{3+} , this state was attained with no infiltration of water into the binding pocket. Upon analysis, the Lu^{3+} coordination environment from the last 2 μ s of the simulations supported that D7, E11, and E14 exhibited bidentate ligation, whereas D3 and W9 displayed monodentate ligation (Table S2). Notably, the total coordination number of Lu^{3+} was found to be 8, which is lower than that of La^{3+} , indicating a less complex coordination environment. Moreover, we observed that the loss in coordination of the N5 residue is compensated by the transformation of D7 residue from monodentate in the initial LBT3- Lu^{3+} structure to bidentate ligation (Figure 3B, inset).

2.4. Free Energy Landscape of LBT3: Ln^{3+} Complexes Revealed by Metadynamics Simulations

The N5 dissociation in the LBT3- La^{3+} complex leads to a wide range of open-pocket conformations in contrast to the binary mode exhibited by the LBT3- Lu^{3+} complex. Additionally, the total CN reaches a value of 10 for La^{3+} in the LBT3-binding pocket, while it remains at 8 for Lu^{3+} . Compared to their coordination numbers in bulk water (9 for La^{3+} and 8 for Lu^{3+}),^[41] the local

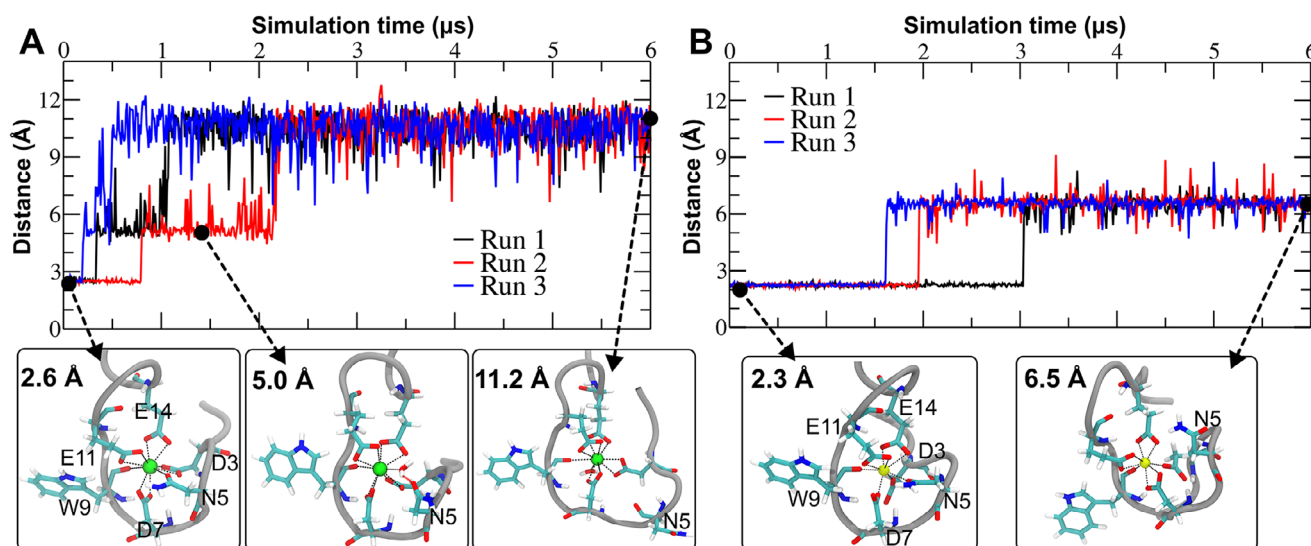


Figure 3. Long-time-scale unbiased MD simulations support the dissociation of N5 in the LBT3- La^{3+} complex. The distance between (A) La^{3+} or (B) Lu^{3+} and the oxygen atom of the carbonyl group on the N5 residue (OD1(N5)) as a function of simulation time for the three parallel runs. The typical structures are inserted with the distances of $\text{Ln(III)}\text{-OD1(N5)}$ provided. The white dotted lines denote the $\text{Ln(III)}\text{-oxygen}$ coordination. $\text{La}^{3+}/\text{Lu}^{3+}$ are colored in green/yellow, respectively, with oxygen/nitrogen/carbon/hydrogen atoms in red/blue/cyan/white, respectively.

binding environment within LBT3 elevates the CN of La^{3+} by 1, with no change for Lu^{3+} . To further validate the calculated CN values that were determined from unbiased AA-MD simulations and to probe the relative energetics of the observed conformations, we conducted metadynamics simulations using two collective variables: the total CN and the distance of $\text{Ln}^{3+}\text{-OD1(N5)}$. Each metadynamics simulation lasted an aggregate of 1.8 μs . The simulations of LBT3-La^{3+} and LBT3-Lu^{3+} complexes converged at 1.7 and 1.6 μs , respectively (Figure S7). Additional details are available in the Supporting Information.

The metadynamics simulations support that La^{3+} favors the coordination environment with $\text{CN} = 10$ over $\text{CN} = 9$, followed by other values of CN (Figure 4A). Detailed analysis of the LBT3-La^{3+} structures derived from the most thermodynamically favorable regions of the free energy landscape corroborates the coordination environment observed with the long-time-scale unbiased simulations. Specifically, D3, D7, E11, and E14 form bidentate ligation with W9 forming monodentate ligation, along with one coordinating water molecule (Figure 4A, Table S1). In comparison, Lu^{3+} energetically favors $\text{CN} = 8$ with the bidentate ligation from D7, E11, and D14 and the monodentate ligation from D3 and W9 (Figure 4B, Table S2). Remarkably, both the long-time-scale unbiased simulation and the metadynamics simulation indicated that the La^{3+} ion in the LBT3-La^{3+} complex has a higher coordination number compared to in bulk water ($\text{CN} = 9$).^[41] However, this elevated CN is not observed for the Lu^{3+} ion, which maintains CN of 8; this coordination is the same as that attained in its hydrated state.

The free energy landscape as a function of $\text{La}^{3+}\text{-OD1(N5)}$ distance was observed to be relatively flat after N5 dissociation (Figure 4A), allowing the LBT3-La^{3+} complex to adopt multiple open-pocket conformations. However, for the LBT3-Lu^{3+} complex, the energy wells are better defined (Figure 4B): the lowest energy state corresponds to the partially dissociated N5 state,

and complete dissociation of N5 was found to be energetically disfavored.

Thermodynamically, a coordination number of 10 versus 8 would seem to suggest an overall weaker interaction between the ion and the ligating residues for the lower coordination environment (Lu^{3+}). However, as shown below, the experimental dissociation constants (K_D) measurements indicate the opposite trend. For the LBT3-La^{3+} complex, interactions between the La^{3+} cation with the ligating residues are weaker, permitting H_2O infiltration. Notably, the LBT3-La^{3+} complex is far more dynamic, leading to larger separation distances and fluctuations (Table S1) relative to the LBT3-Lu^{3+} complex (Table S2). Also, La^{3+} is larger in size and can accommodate more ligands to marginally compensate for the weaker interactions, resulting in the higher CN. In contrast, the LBT3-Lu^{3+} complex exhibits stronger interactions, resulting in a more rigid structure with less fluctuations in ligand positions.

2.5. Intramolecular H-Bonding and LBT3-Lu^{3+} Complex Interlocking

The tight binding of the Lu^{3+} complex is unequivocally linked to the absence of complete dissociation of the N5 residue. To delve deeper into this phenomenon, we examined the simulation snapshots of both complexes following N5 dissociation (Figure 5A). Remarkably, our analysis revealed that in the LBT3-Lu^{3+} complex, complete N5 dissociation is impeded by an inter-arm hydrogen bond (H-bond) between the N5 and E14 residues. This intramolecular H-bond effectively secures the complex, encapsulating the Lu^{3+} cation tightly. The occurrence of this H-bond was calculated to be 62.0%, 62.3%, and 63.4% of the simulation times for the three parallel runs. Conversely, such a phenomenon is not observed in the LBT3-La^{3+} complex,

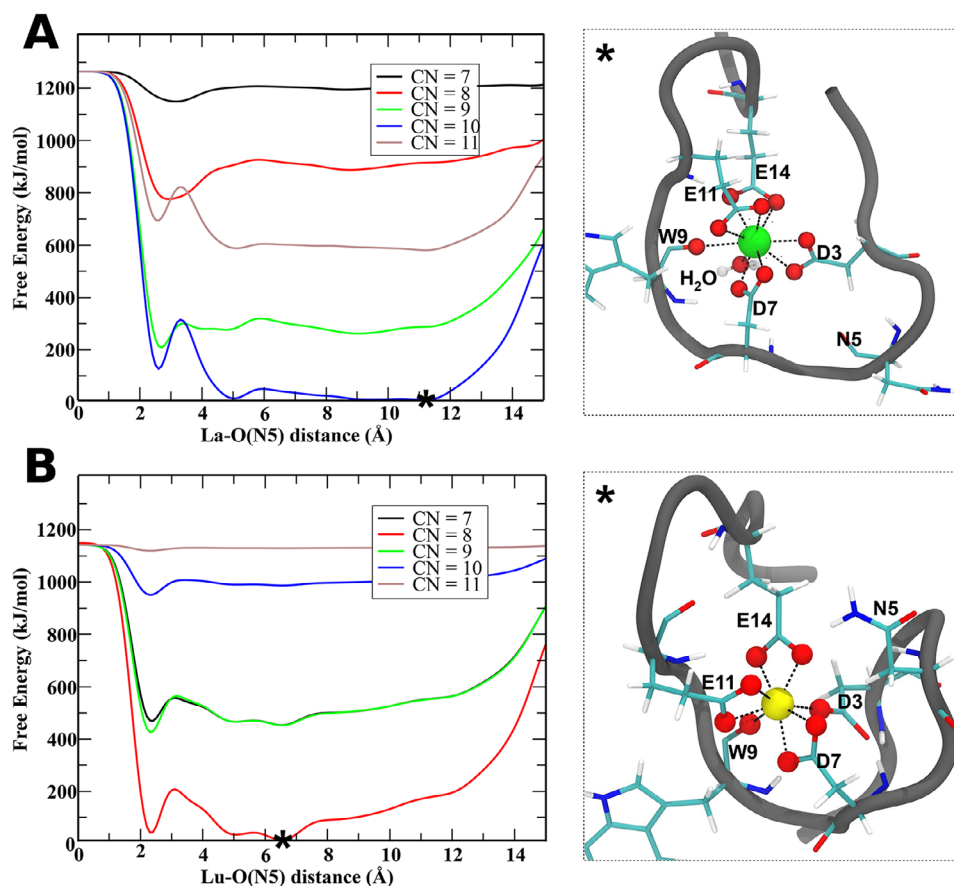


Figure 4. Metadynamics simulations support CN = 10/8 of $\text{La}^{3+}/\text{Lu}^{3+}$ when complexing with LBT3, respectively. (A) CN = 10 for La^{3+} is energetically favored with the optimal La^{3+} -OD1(N5) distance of around 11.3 Å. The most stable structure (indicated by *) is inserted on the right, which demonstrates that N5 is dissociated, and the bidentate binding dominates for D3, D7, E11, and E14. (B) CN = 8 for Lu^{3+} is the most stable with the optimal Lu^{3+} -OD1(N5) distance of 6.5 Å. The most stable structure (indicated by *) is inserted, demonstrating that N5 is partially dissociated and that the monodentate binding is favored for D3, but bidentate binding for D7, E11, and E14. The black dotted lines denote the Ln^{3+} -oxygen coordination. The corresponding rotation animations are provided in the Supporting Information.

primarily due to the larger size of the La^{3+} cation, which results in a wider binding pocket with greater distance between the N5 and E14 residues, impeding the formation of the H-bond. Thus, the N5 residue serves as a gatekeeper for smaller Ln^{3+} cations like Lu^{3+} , for which it remains closed, but opens widely for larger cations like La^{3+} due to the absence of intramolecular H-bond.

We additionally validate the presence of the intermolecular H-bond by conducting ^1H proton exchange NMR measurements. In these experiments, only ^1H signals that are chemically exchanging with water—and thus are solvent accessible—are observed. This NMR technique enables experimental validation of water interactions with residues with molecular specificity. The sidechain amide hydrogens of the N5 residue (N5-HD_{2x} and N5-HD_{2y}) participated in proton exchange with water for the LBT3:La^{3+} complex as they were exposed to the bulk water upon complete dissociation (Figure S8). Intriguingly, this proton exchange was only observed for one of the N5 side chain amide protons (HD_{2y}) for the LBT3:Lu^{3+} complex. This observation is indicative of the inter-arm H-bond between N5 and E14 corresponding to the closed gate for the LBT3:Lu^{3+} complex (Figure 5A), where one of the sidechain protons of N5 resides inside the binding pocket, while the other is solvent-exposed.

Proton chemical exchange was also detected for the backbone amide protons in both Ln^{3+} complexes (Figure S8,C). We observed proton exchange for the N5 residue only in the LBT3:La^{3+} complex. This finding reaffirms the notion of a population with a completely dissociated N5 residue, in which the backbone amide proton is solvated by water. Furthermore, a significant difference in the amide proton hydration of neighboring residues such as N6, D7, and W9 was observed between the LBT3:La^{3+} and LBT3:Lu^{3+} complexes. Proton exchange for these residues was prevalent only in the LBT3:La^{3+} complex. We speculate this behavior to be a result of the change in backbone orientation associated with the N5 dissociation. To confirm this hypothesis, we calculated the minimum distance between water and the backbone amide protons of N5, N6, D7, and W9 in the last 2 μs from the AA-MD simulations. The simulation analysis agreed with the experimental results in which the minimum distances were found to be lower for the LBT3:La^{3+} complex (Figure S9), indicating a solvated environment. Additionally, the simulations show that the lower distances observed were a consequence of N5 dissociation (Figures S8 and S9). These differences suggest a varied interaction of backbone amide protons with solvent water molecules, emphasizing that N5

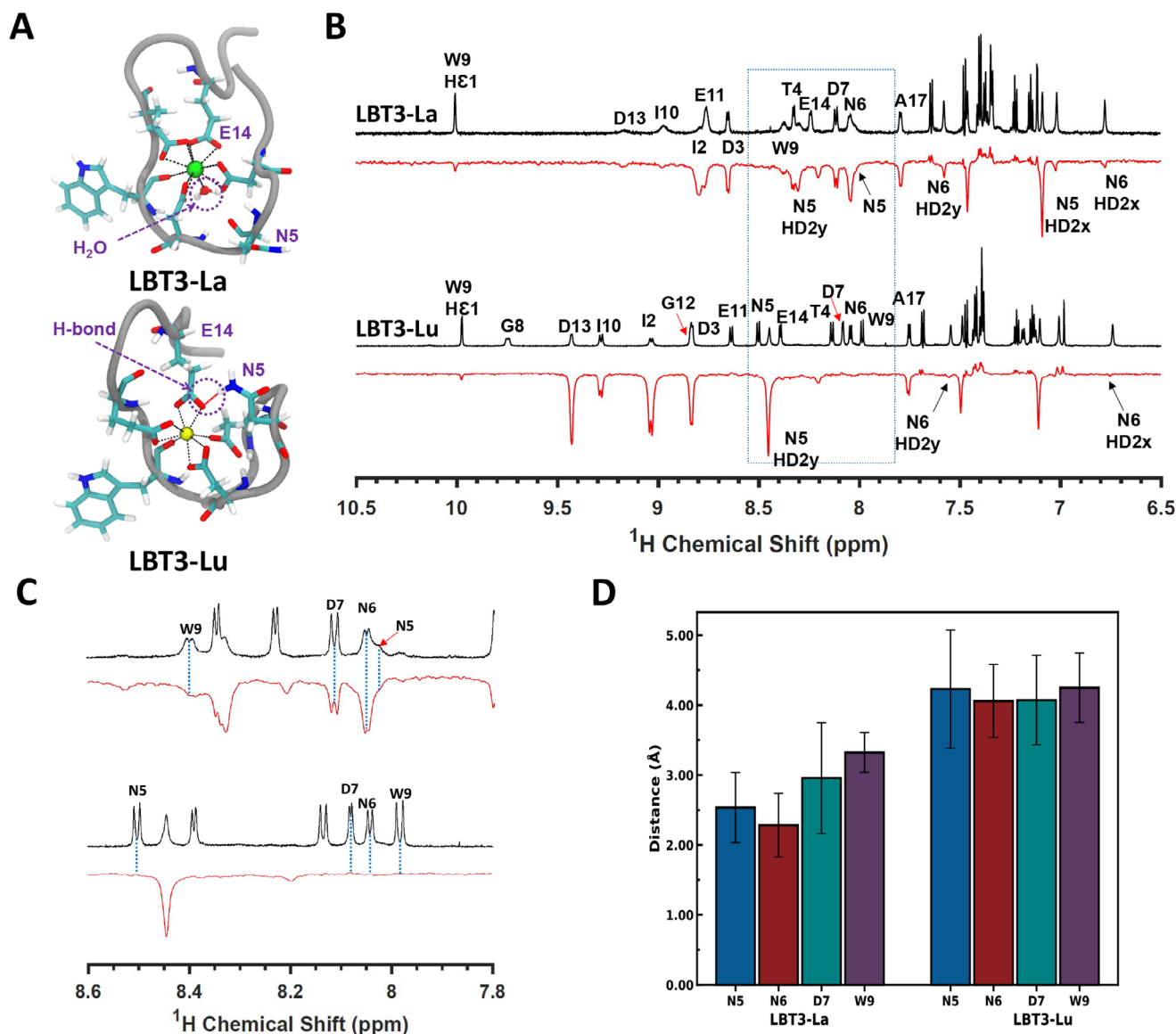


Figure 5. Impact of N5 dissociation effects on complex interlocking. (A) Simulation snapshots depict the exclusive presence of intramolecular hydrogen bonding (red dotted lines) between the N5 arm and the E14 residue within the LBT3-Lu³⁺ complex. (B) Comparison of ¹H single-pulse (black) and ¹H proton exchange (red) NMR spectra of LBT3-La³⁺ and LBT3-Lu³⁺, where ¹H signals present in the proton exchange spectra are exchanging with water molecules over 200 ms. (C) Expanded view highlighting key differences in proton exchange of residues N5, N6, D7, and W9 between LBT3-La³⁺ and LBT3-Lu³⁺ complexes. (D) Minimum distances between backbone amide proton of residues N5, N6, D7, and W9 and neighboring water molecules for LBT3-La³⁺ and LBT3-Lu³⁺ from atomistic simulations. Error bars represent the standard deviation about the mean for three different simulations.

dissociation modulates the conformational dynamics of the LBT3:Ln³⁺ complex, thereby affecting the water accessibility of neighboring residues.

2.6. Gatekeeping Mechanism's Role in Selectivity: Insights From N5 Mutation

To underscore the gating mechanism's significance in selective binding of Ln³⁺, we mutated the N5 asparagine residue in LBT3 to a D5 aspartic acid. The N5D mutation introduces a stronger charged ligating residue while eliminating the inter-arm hydrogen bond. The thermodynamic binding constants (K_D) obtained from luminescence spectroscopy for LBT3 and LBT3_N5D pep-

tides are compared in Figure 6A and listed in Table S3. For LBT3, across the lanthanide series, the dissociation constant decreased sharply for the lighter lanthanides and then showed a minor increase from Ho³⁺ to Lu³⁺. We attribute the minor variation from Ho³⁺ to Lu³⁺ to the stabilizing intramolecular H-bond, while the major pronounced variations observed from La³⁺ to Eu³⁺ arise from a dissociated N5, water infiltration, and multiple open-pocket conformations. Notably, there is a 100-fold difference between the measured K_D values of the LBT3-Lu³⁺ (139 nM) and LBT3-La³⁺ (14,211 nM) complexes. In contrast, the LBT3_N5D mutant loses the ability to differentiate between smaller and larger Ln³⁺ cations, eliminating selectivity. The negatively charged D5 residue enhances the binding affinity for larger Ln³⁺ ions (La³⁺, Ce³⁺, and Nd³⁺) due to favorable electrostatic

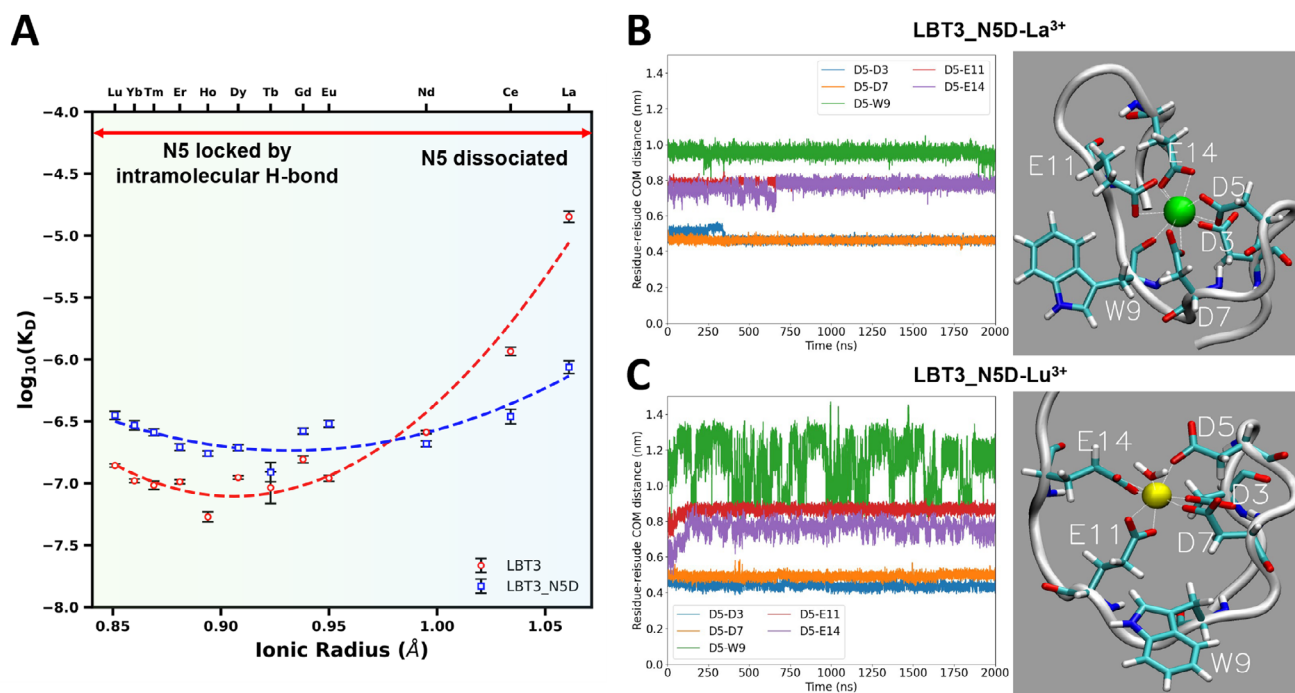


Figure 6. (A) Dissociation constants (K_D) of LBT3- Ln^{3+} complexes and LBT3_N5D- Ln^{3+} complexes by luminescence spectroscopy. Error bars represent the standard deviation of triplicate measurements. (B) Time trajectory of the center of mass (COM) distance between D5 and other ligating residues (D3, D7, W9, and E11) in the LBT3_N5D- La^{3+} complex. A snapshot of the binding conformation at $t = 2000$ ns is shown on the right. (C) Time trajectory of the center of mass (COM) distance between D5 and ligating residues (D3, D7, W9, and E11) in the LBT3_N5D- Lu^{3+} complex. A snapshot of the binding conformation at $t = 2000$ ns is shown on the right.

interactions, whereas binding affinity decreases for smaller Ln^{3+} ions. As a result, the K_D ratio of $\text{La}^{3+}/\text{Lu}^{3+}$ drops from 100-fold in LBT3 to just 2.5-fold in LBT3_N5D, highlighting the significance of the gatekeeping N5 residue in elevated REE selectivity.

MD simulations provide key insights into the conformational changes induced by the N5D mutation. In the LBT3_N5D- La^{3+} complex, D5 forms a strong bidentate ligand, unlike the weaker N5 residue in LBT3. Ligating residues D3 and W9 exhibit monodentate binding, whereas D7, E11, and E14 coordinate in a bidentate manner (Figure S10). Throughout the simulation, the residue–residue center of mass (COM) distances between ligating residues remain stable (Figure 6B), while no water infiltration is observed, indicating an absence of electrostatic repulsion due to the larger pocket size.

In contrast, the LBT3_N5D- Lu^{3+} complex exhibits significant structural disruption. The smaller pocket size brings D5 in close proximity to the E11 and E14 residues, leading to electrostatic repulsion (Figure 6C). This repulsion destabilizes the weaker W9 residue, causing its dissociation from the pocket and, significantly, allowing water infiltration. Additionally, in this mutant complex, the D3, D5, D7, and W9 residues adopt monodentate binding, while the E11 and E14 residues maintain bidentate coordination (Figure S11). These disruptive factors contribute to the increase in K_D values from 139 nM in LBT3 to 353 nM observed for the mutant peptide. This finding underscores the critical role of the N5 residue in imparting size-based selectivity. Despite being a weaker binding residue, its ability to act as a conformational gate through an inter-arm hydrogen bond—regulated by Ln^{3+} size—enhances binding affinity for smaller (heavier) Ln^{3+}

ions, thereby increasing selectivity. Thus, N5 functions as a gating residue essential for distinguishing between lighter and heavier lanthanide cations.

3. Conclusion

This study provides a comprehensive understanding of the structural and dynamic mechanisms underlying the selective binding of Ln^{3+} cations by the LBT3 peptide. Using a synergistic combination of NMR spectroscopy and classical and metadynamics AA-MD simulations, we demonstrated that LBT3's binding affinity and selectivity for Ln^{3+} cations are closely tied to its conformational dynamics and the gating role of the N5 residue. The binding affinity of LBT3 to Ln^{3+} cations was observed by measuring changes in ^1H chemical shifts, indicative of conformational changes upon binding, as evidenced by solution-state ^1H single-pulse NMR titration experiments. Additionally, we observed unique chemical exchange kinetics between the bound and unbound states of LBT3, with fast exchange for La^{3+} and slow exchange for Lu^{3+} , highlighting its ability to distinguish Ln^{3+} ions.

Our structural analysis revealed that the N5 residue imparts selectivity across the Ln^{3+} series by adopting many energetically similar conformations in the open gate state for larger cations, while maintaining more restricted conformations in the closed gate state for smaller cations. The restricted conformations for smaller REE cations like Lu^{3+} arise from an intramolecular hydrogen bond between N5 and E14, which effectively locks

the complex and prevents water penetration. Despite being a weaker binding residue, this gatekeeper function of N5 was critical for achieving selectivity across the Ln^{3+} series. The introduction of an N5D mutation, replacing the asparagine residue with a charged aspartic acid residue, eliminated LBT3's size-based selectivity while maintaining high binding affinity. This finding underscores the pivotal role of N5 in modulating pocket dynamics and regulating cation hydration, which are essential for size-based discrimination of Ln^{3+} ions. Overall, this work highlights the interplay between peptide structure, Ln^{3+} cation size, and water, elucidating the underlying mechanisms governing lanthanide binding selectivity. These insights provide rational design principles for tailoring the sequences of LBT peptides to achieve enhanced lanthanide binding selectivity.

Supporting Information

The Supporting Information includes detailed protocols for multidimensional solution-state NMR measurements and structure determination, as well as descriptions of computational methodologies for all-atom molecular dynamics (AA-MD) simulations and well-tempered metadynamics. Procedures for luminescence spectroscopy are also described. Supplementary NMR and simulation data that corroborate our findings are included. The authors have cited additional references within the Supporting Information.^[42–62]

Acknowledgements

The authors gratefully acknowledge the U.S. Department of Energy (DOE) under the Basic Energy Sciences award number DE-SC0022240. NMR measurements were acquired in the City University of New York Advanced Science Research Center NMR facility. The MALDI MS instrument used for peptide characterization was supported by the U.S. National Institutes of Health (NIH) award S10 OD030460. The authors acknowledge the ACCESS allocation grant (MCB200101) in part for the availability of high-performance computing resources.

Conflict of Interests

The authors declare no conflict of interest.

Data Availability Statement

NMR structures of the LBT3- La^{3+} complex have been validated and uploaded to the Protein Data Bank (PDB ID: 9CEQ, BMRB ID: 31181).

Keywords: bioseparation · lanthanide-binding tags · lanthanide coordination · rare earth elements · selectivity

- [1] J. C. G. Bünzli, C. Piguet, *Chem. Soc. Rev.* **2005**, 34, 1048.
- [2] N. C. Martinez-Gomez, H. N. Vu, E. Skovran, *Inorg. Chem.* **2016**, 55, 10083.
- [3] D. Parker, E. A. Suturina, I. Kuprov, N. F. Chilton, *Acc. Chem. Res.* **2020**, 53, 1520.
- [4] *Critical Mineral Resources of the United States : Economic and Environmental Geology and Prospects for Future Supply* (Eds: K. J. Schulz, J. H. DeYoung Jr., R. R. Seal, D. Bradley), U.S. Geological Survey, Reston **2017**.^{[bib>}
- [5] *The Rare Earth Elements: Fundamentals and Applications* (Ed: D. A. Atwood), Wiley, Germany **2013**.
- [6] *Rare Earth Materials* (Ed: A. R. Jha), CRC Press, Boca Raton **2014**.
- [7] *Handbook of Rare Earth Elements* (Ed: A. Golloch), De Gruyter, Berlin **2022**.
- [8] J. Lucas, P. Lucas, T. Le Mercier, A. Rollat, W. Davenport, *Rare Earths: Science, Technology, Production and Use*, Elsevier, Amsterdam **2014**.
- [9] H. Paulick, E. Machacek, *Resources Policy* **2017**, 52, 134.
- [10] R. D. Shannon, *Acta Crystallogr. A* **1976**, 32, 751.
- [11] F. Xie, T. A. Zhang, D. Dreisinger, F. Doyle, *Miner. Eng.* **2014**, 56, 10.
- [12] P. Zapp, A. Schreiber, J. Marx, W. Kuckshinrichs, *MRS Bull.* **2022**, 47, 267.
- [13] J. A. Mattocks, J. A. Cotruvo, *Chem. Soc. Rev.* **2020**, 49, 8315.
- [14] Q. Ye, D. Wang, N. Wei, *Trends Biotechnol.* **2023**, 42, 575.
- [15] X. Xie, X. Tan, Y. Yu, Y. Li, P. Wang, Y. Liang, Y. Yan, *J. Hazard. Mater.* **2022**, 424, 127642.
- [16] A. Brewer, E. Chang, D. M. Park, T. Kou, Y. Li, L. N. Lammers, Y. Jiao, *Environ. Sci. Technol.* **2019**, 53, 7714.
- [17] D. Park, A. Middleton, R. Smith, G. Deblonde, D. Laudal, N. Theaker, H. Hsu-Kim, Y. Jiao, *Sep. Purif. Technol.* **2020**, 241, 116726.
- [18] D. M. Park, A. Brewer, D. W. Reed, L. N. Lammers, Y. Jiao, *Environ. Sci. Technol.* **2017**, 51, 13471.
- [19] D. M. Park, D. W. Reed, M. C. Yung, A. Eslamimanesh, M. M. Lencka, A. Anderko, Y. Fujita, R. E. Riman, A. Navrotsky, Y. Jiao, *Environ. Sci. Technol.* **2016**, 50, 2735.
- [20] P. K. R. Tay, A. Manjula-Basavanna, N. S. Joshi, *Green Chem.* **2018**, 20, 3512.
- [21] J. A. Cotruvo Jr, E. R. Featherston, J. A. Mattocks, J. V. Ho, T. N. Laremore, *J. Am. Chem. Soc.* **2018**, 140, 15056–15061.
- [22] G. J.-P. Deblonde, J. A. Mattocks, D. M. Park, D. W. Reed, J. A. Cotruvo Jr, Y. Jiao, *Inorg. Chem.* **2020**, 59, 11855.
- [23] Q. Ye, X. Jin, B. Zhu, H. Gao, N. Wei, *Environ. Sci. Technol.* **2023**, 57, 4276.
- [24] X. Xie, K. Yang, Y. Lu, Y. Li, J. Yan, J. Huang, L. Xu, M. Yang, Y. Yan, *J. Hazard. Mater.* **2022**, 438, 129561.
- [25] M. Gut, T. Wilhelm, O. Beniston, S. Ogundipe, C. C. Kuo, K. Nguyen, A. Furst, *Adv. Mater.* **2025**, 37, 2412607.
- [26] Z. Hussain, S. Kim, J. Cho, G. Sim, Y. Park, I. Kwon, *Adv. Funct. Mater.* **2022**, 32, 2109158.
- [27] J. A. Mattocks, J. J. Jung, C. Y. Lin, Z. Dong, N. H. Yennawar, E. R. Featherston, C. S. Kang-Yun, T. A. Hamilton, D. M. Park, A. K. Boal, J. A. Cotruvo, *Nature* **2023**, 618, 87.
- [28] Z. Dong, J. A. Mattocks, G. J.-P. Deblonde, D. Hu, Y. Jiao, J. A. Cotruvo Jr, D. M. Park, *ACS Cent. Sci.* **2021**, 7, 1798.
- [29] G. Verma, J. Hostert, A. A. Summerville, A. S. Robang, R. Garcia Carcamo, A. K. Paravastu, R. B. Getman, C. E. Duval, J. Renner, *ACS Appl. Mater. Interfaces* **2024**, 16, 16912.
- [30] J. D. Hostert, M. R. Sepesy, C. E. Duval, J. N. Renner, *Soft Matter* **2023**, 19, 2823.
- [31] S. M. Gutenthaler, S. Tsushima, R. Steudtner, M. Gailer, A. Hoffmann-Röder, B. Drobot, L. J. Daumann, *Inorg. Chem. Front.* **2022**, 9, 4009.
- [32] M. Nitz, K. J. Franz, R. L. Maglathlin, B. Imperiali, *ChemBioChem* **2003**, 4, 272.
- [33] U. Cho, J. K. Chen, *Cell Chem. Biol.* **2020**, 27, 921.
- [34] B. R. Sculimbrene, B. Imperiali, *J. Am. Chem. Soc.* **2006**, 128, 7346.
- [35] T. W. Victor, K. H. O'Toole, L. M. Easton, M. Ge, R. J. Smith, X. Huang, H. Yan, Y. S. Chu, S. Chen, D. Gursoy, M. Ralle, B. Imperiali, K. N. Allen, L. M. Miller, *J. Am. Chem. Soc.* **2020**, 142, 2145.
- [36] K. J. Franz, M. Nitz, B. Imperiali, *ChemBioChem* **2003**, 4, 265.
- [37] K. D. Daughtry, L. J. Martin, A. Sarraju, B. Imperiali, K. N. Allen, *ChemBioChem* **2012**, 13, 2567.
- [38] L. E. O. Macias, F. Jiménez-Ángeles, J. G. Marmorstein, Y. Wang, S. A. Crane, K. T. Surabh, P. Sun, B. Sapkota, E. Hummingbird, W. Jung, B. Qiao, D. Lee, I. J. Dmochowski, R. J. Messinger, M. L. Schlossman, C. De La Fuente-Nunez, R. Radhakrishnan, E. J. Petersson, M. O. De La Cruz,

- W. Bu, M. Bera, B. Lin, R. S. Tu, K. J. Stebe, C. Maldarelli, *Proc Natl Acad Sci U S A* **2024**, *121*, e2411763121.
- [39] M. Nitz, M. Sherawat, K. J. Franz, E. Peisach, K. N. Allen, B. Imperiali, *Angew. Chem., Int. Ed.* **2004**, *43*, 3682.
- [40] T. Hatanaka, N. Kikkawa, A. Matsugami, Y. Hosokawa, F. Hayashi, N. Ishida, *Sci. Rep.* **2020**, *10*, 19468.
- [41] B. Qiao, S. Skanthakumar, L. Soderholm, *J. Chem. Theory Comput.* **2018**, *14*, 1781.
- [42] S. P. Skinner, R. H. Fogh, W. Boucher, T. J. Ragan, L. G. Mureddu, G. W. Vuister, *J. Biomol. NMR* **2016**, *66*, 111.
- [43] Y. Shen, A. Bax, *J. Biomol. NMR* **2013**, *56*, 227.
- [44] D. Gottstein, D. K. Kirchner, P. Güntert, *J. Biomol. NMR* **2012**, *52*, 351.
- [45] B. Hess, C. Kutzner, D. van der Spoel, E. Lindahl, *J. Chem. Theory Comput.* **2008**, *4*, 435.
- [46] J. Huang, S. Rauscher, G. Nawrocki, T. Ran, M. Feig, B. L. de Groot, H. Grubmüller, A. D. MacKerell, *Nat. Methods* **2017**, *14*, 71.
- [47] W. Humphrey, A. Dalke, K. Schulten, *J Mol Graph* **1996**, *14*, 33.
- [48] A. D. MacKerell, D. Bashford, M. Bellott, R. L. Dunbrack, J. D. Evanseck, M. J. Field, S. Fischer, J. Gao, H. Guo, S. Ha, D. Joseph-McCarthy, L. Kuchnir, K. Kuczera, F. T. K. Lau, C. Mattos, S. Michnick, T. Ngo, D. T. Nguyen, B. Prodhom, W. E. Reiher, B. Roux, M. Schlenkrich, J. C. Smith, R. Stote, J. Straub, M. Watanabe, J. Wiórkiewicz-Kuczera, D. Yin, M. Karplus, *J. Phys. Chem. B* **1998**, *102*, 3586.
- [49] S. Miyamoto, P. A. Kollman, *J. Comput. Chem.* **1992**, *13*, 952.
- [50] U. Essmann, L. Perera, M. L. Berkowitz, T. Darden, H. Lee, L. G. Pedersen, *J. Chem. Phys.* **1995**, *103*, 8577.
- [51] T. Darden, D. York, L. Pedersen, *J. Chem. Phys.* **1993**, *98*, 10089.
- [52] J. Lee, X. Cheng, J. M. Swails, M. S. Yeom, P. K. Eastman, J. A. Lemkul, S. Wei, J. Buckner, J. C. Jeong, Y. Qi, S. Jo, V. S. Pande, D. A. Case, C. L. Brooks, A. D. MacKerell, J. B. Klauda, W. Im, *J. Chem. Theory Comput.* **2016**, *12*, 405.
- [53] B. Panganiban, B. Qiao, T. Jiang, C. DelRe, M. M. Obadia, T. D. Nguyen, A. A. A. Smith, A. Hall, I. Sit, M. G. Crosby, P. B. Dennis, E. Drockenmuller, M. O. De La Cruz, T. Xu, *Science* **2018**, *359*, 1239.
- [54] B. Qiao, L. Lopez, M. Olvera De La Cruz, *J. Phys. Chem. B* **2019**, *123*, 3907.
- [55] B. Qiao, F. Jiménez-Ángeles, T. D. Nguyen, M. O. De, La Cruz, *Proc Natl Acad Sci U S A* **2019**, *116*, 19274.
- [56] B. Qiao, M. O. De La Cruz, *ACS Nano* **2020**, *14*, 10616.
- [57] H. Sun, B. Qiao, W. Choi, N. Hampu, N. C. McCallum, M. P. Thompson, J. Oktawiec, S. Weigand, O. M. Ebrahim, M. O. De La Cruz, N. C. Gianneschi, *ACS Cent. Sci.* **2021**, *7*, 2063.
- [58] T. Jiang, A. Hall, M. Eres, Z. Hemmatian, B. Qiao, Y. Zhou, Z. Ruan, A. D. Couse, W. T. Heller, H. Huang, M. O. de la Cruz, M. Rolandi, T. Xu, *Nature* **2020**, *577*, 216.
- [59] M. Bonomi, D. Branduardi, G. Bussi, C. Camilloni, D. Provasi, P. Raiteri, D. Donadio, F. Marinelli, F. Pietrucci, R. A. Broglia, M. Parrinello, *Comput. Phys. Commun.* **2009**, *180*, 1961.
- [60] A. Barducci, M. Bonomi, M. Parrinello, *Wiley Interdiscip Rev Comput Mol Sci* **2011**, *1*, 826.
- [61] A. Barducci, G. Bussi, M. Parrinello, *Phys. Rev. Lett.* **2008**, *100*, 020603.
- [62] P. Raiteri, A. Laio, F. Luigi Gervasio, C. Micheletti, M. Parrinello, *J. Phys. Chem. B* **2005**, *110*, 3533.

Manuscript received: April 22, 2025

Version of record online: May 9, 2025